Proper motions with Subaru I. Methods and a first sample in the Subaru Deep Field

Michael W. RICHMOND
Physics Department, Rochester Institute of Technology,
Rochester, NY 14623, USA
mwrsps@rit.edu
Tomoki MOROKUMA
Optical and Infrared Astronomy Division, National Astronomical Observatory of Japan,
2-21-1 Osawa, Mitaka, Tokyo 181-8588, Japan
tomoki.morokuma@nao.ac.jp
Mamoru DOI
Institute of Astronomy, Graduate School of Science, University of Tokyo,
2-21-1, Osawa, Mitaka, Tokyo 181-0015, Japan
doi@ioa.s.u-tokyo.ac.jp
Yutaka KOMIYAMA
Optical and Infrared Astronomy Division, National Astronomical Observatory of Japan,
2-21-1 Osawa, Mitaka, Tokyo 181-8588, Japan
komiyama@subaru.naoj.org
Naoki YASUDA
Institute for Cosmic Ray Research, University of Tokyo,
5-1-5 Kashiwa-no-Ha, Kashiwa, Chiba 277-8582, Japan
yasuda@icrr.u-tokyo.ac.jp
Sadanori OKAMURA
Department of Astronomy and Research Center for the Early Universe, School of Science, University of Tokyo
7-3-1 Hongo, Bunkyo, Tokyo 113-0033, Japan
okamura@astron.s.u-tokyo.ac.jp
and
Avishay Gal-Yam
Benoziyo Center for Astrophysics, Weizmann Institute of Science, 76100 Rehovot, Israel
avishay.gal-yam@weizmann.ac.il

(Received ; accepted)

Abstract

We search for stars with proper motions in a set of twenty deep Subaru images, covering about 0.28 square degrees to a depth of $i' \simeq 25$, taken over a span of six years. In this paper, we describe in detail our reduction and techniques to identify moving objects. We present a first sample of 99 stars with motions of high significance, and discuss briefly the populations from which they are likely drawn. Based on photometry and motions alone, we expect that 9 of the candidates may be white dwarfs. We also find a group of stars which may be extremely metal-poor subdwarfs in the halo.

Key words: stars: kinematics — Galaxy: kinematics and dynamics — Galaxy: structure

1. Introduction

The basic structure of our Milky Way galaxy seems clear: a thin disk of young stars, gas and dust circles the center quietly, immersed within a thicker disk of older stars. Both disks sit inside a nearly spherical halo of very old, metal-poor stars which do not share the overall rotation of the disks. Surrounding everything is an extended distribution of dark matter. Our knowledge of the details within this big picture, on the other hand, is not so clear. Recent large-scale projects, such as the Sloan Digital Sky Survey, have measured the properties of high-luminosity stars throughout the halo (see, for example, Yanny et al. 2000, and Juric et al. 2008), while the rapid development of infrared detectors has allowed projects such as the Two Micron All Sky Survey (Skrutskie et al. 2006) and Spitzer Space Telescope (Patel & Spath 2004) to pierce the dusty disks and measure the properties of their stars. Nonetheless, some portions of the Milky Way remain largely unexplored.

In particular, we know little of the low-mass, low-luminosity stars of the halo. The white dwarfs and metal-poor subdwarfs of the halo glow so faintly, from so great a distance, that they are rarely seen and more rarely recognized. As a recent review (Reid 2005) points out, however, these shy and elusive stars may dominate the microlensing events observed towards the Galactic bulge and the Magellanic Clouds.

There are two ways to search for these stars: cover a very large area on the sky to a shallow depth, or use a "pencil-beam" survey to examine a tiny region much more deeply.

The first approach (see, for example, Oppenheimer et al. 2001 and Carollo et al. 2006) will find objects in many directions, but only out to a small distance from the Sun; the second approach (see, for example, Mendez 2002, Nelson et al. 2002, and Kalirai et al. 2004) probes farther into the halo, but only in a specific direction. One way to characterize surveys is to combine their area with the distance out to which they would detect some specific star to generate an "effective volume" for that type of star. In Table 1, we compare the projects mentioned above by this metric, using a star of absolute magnitude $M_V = 16.5$, appropriate for a cool white dwarf. We assumed a color $(V-R) = 0.5$ to convert limiting magnitudes for R-based surveys to V-band.

Our project could be described as a "pencil-beam" survey, but it uses a very thick pencil. We examine images in the area of the Subaru Deep Field (SDF) (Kashikawa et al. 2004) acquired over a period of six years to search for moving objects. These images were acquired primarily to study high-redshift galaxies (Nagao et al. 2004, Shimasaku et al. 2006), but have also been used to find high-redshift supernovae (Poznanski et al. 2007). The images are nearly as deep as those in some HST-based surveys, but cover a significantly wider area, yielding a large effective volume. We can refer to the SDF catalogs compiled by Kashikawa et al. (2004) and Richmond (2005) for information on our candidates in multiple passbands (B, V, R_c, i' and z'). Unlike most other pencil-beam surveys, we have measurements at many epochs: our dataset contains images taken on 20 nights. We can therefore measure the proper motion of our candidates very well, and place strong constraints on the uncertainties in our measurements.

This paper is the first in a series on proper motions in several small fields studied with Subaru. We will concentrate on techniques, leaving detailed analysis of the results for later papers. In Section 2, we describe the observations, their reductions, and the combination of individual frames into a single combined image for each night. In Section 3, we walk through our procedure for finding moving objects, and discuss our criteria for separating good candidates from bogus ones; we end up with a first sample of stars which have very well measured proper motions. In Section 4, we compute the reduced proper motions for objects in this sample, and compare their properties to those of objects drawn from a simulated survey of our field. Finally, in Section 5, we list our plans for future work on this dataset, and in other fields with multiple epochs of deep Subaru imaging.

Astronomers at the Observatoire de Besançon have created a model of the stellar populations in the Milky Way (Robin et al. 2003) with a very convenient web-based interface[1]. The model consists of four populations of stars – thin disk, thick disk, spheroid, outer bulge (the innermost portions of the Milky Way are poorly constrained) – plus white dwarfs added to each component separately. The parameters of each component are adjusted to produce the best fit to the observed stellar populations and their dynamics. Recent work by Ibata et al. (2007) finds that the Besançon model does a very good job of reproducing observed star counts in two of three deep fields down to $i_0 = 24$. Those authors criticized the Besançon populations for being too sharply defined, forcing them to smooth the model colors by small amounts (~ 0.10 mag) in order to match observed color-magnitude diagrams. However, since our main concern is to classify objects very broadly using a mixture of kinematics, magnitudes and colors, we will adopt the Besançon model and use it as a reference throughout this paper to help us interpret properties of our sample.

[1] http://bison.obs-besancon.fr/modele

2. Observations

The SDF is a region at high galactic latitude ($l = 37\overset{\circ}{.}6, b = +82\overset{\circ}{.}6$) roughly half a degree on a side. Kashikawa et al. (2004) describe very deep optical images taken with the Subaru 8.2-meter telescope and Suprime-Cam camera (Miyazaki et al. 2002). We investigated this region using a set of i'-band images with shorter exposure times. Table 2 lists the date for all nights used in our analysis. Note that our images taken on 2003 April 30 had a shorter exposure time than the rest; since these images also had some of the worst seeing, we gave those measurements very little weight in the final proper motion calculations. We split the images taken on the night of 2006 May 3 into two sets and treated each independently, as if taken on different nights. Since the data taken on 2007 Feb 15 had the best seeing and the largest number of detected objects, we adopted it as the fiducial set for matching (see Section 3).

During each night of observing, we took a series of short (typically 180-second to 360-second) exposures, shifting the telescope position slightly to fill in small gaps between the ten CCDs on the focal plane. Using the *SDFRED* package (Ouchi et al. 2004) and NEKO software (Yagi et al. 2002), we followed the procedures described in section 4 of Kashikawa et al. (2004) to turn all the raw frames taken during the night into a single, large mosaic. Briefly, we cleaned the raw images by subtracting a bias deduced from the overscan regions and dividing by a normalized flatfield frame made from a median of many night-time target images. Using the parameters derived in Miyazaki et al. (2002), we corrected for optical distortions in the focal plane. Images from all chips were convolved to form a uniform point-spread function (PSF) across the entire array. We determined a sky background by calculating the local sky at a series of grid points spaced at intervals of roughly 51 arcseconds and using bi-linear interpolation between the grid points; we then subtracted this sky background from each image. We used stars shared by adjacent CCDs to determine the weights to use when combining data from individual images to make the final mosaic. The result for each night is one (or, in the case of 2006 May 3, two) large image covering the entire SDF.

The quality of final combined images varied from night to night. The Full Width at Half Maximum (FWHM) ranged from $0\overset{''}{.}75$ to $1\overset{''}{.}30$, but, since the plate scale was $0\overset{''}{.}202$ per pixel, no data was undersampled. The limiting magnitude also varied with the conditions, but was usually $i' \sim 25.5$.

3. Searching for candidates with proper motion

Selecting objects with proper motions from a set of images requires several steps: finding and measuring the properties of stars in individual images, matching stars found at differ-

Table 1. Effective volumes, for $M_V = +16.5$

Survey	Area (sq.deg.)	limiting mag V	volume (pc^3)
Oppenheimer et al.	4165	19.8	80000
Carollo et al.	1150	20	15000
Nelson et al.	0.021	26.5	2100
Mendez	0.0013	26.0	64
Kalirai et al.	0.0031	29	9800
this work	0.28	26	14000

Table 2. Observations of the SDF in i'-band

UT Date	Julian Date - 2,450,000	Exptime (seconds)
2001 April 25	2024.34	3600
2001 May 20	2049.44	3240
2002 April 12	2376.44	9780
2002 May 7	2401.52	5670
2003 April 1	2730.43	12330
2003 April 3	2732.29	2730
2003 April 25	2754.42	4800
2003 April 26	2755.36	4680
2003 April 30	2759.60	964
2003 May 1	2760.39	4583
2005 March 5	3434.54	5100
2005 March 6	3435.54	5400
2006 May 3(a)	3858.41	3000
2006 May 3(b)	3858.52	2400
2007 February 13	4144.59	2700
2007 February 14	4145.59	4200
2007 February 15	4146.59	4500
2007 February 16	4147.60	3600
2007 May 16	4236.32	4180
2007 May 17	4237.27	3780

ent epochs, computing the change in position of each star over time, and deciding which changes are due to real movement. We will now describe these steps in detail.

In order to find star-like objects in each image, we used the "stars" program within the *XVista* package (Treffers & Richmond 1989)[2]. The position of each object was calculated by fitting a gaussian to the background-subtracted, intensity-weighted marginal sums in each direction (see Stone (1989) for details).

It is not crucial to separate stars from galaxies at this early stage, since we will later discard any objects which do not move significantly; therefore, we accepted any object with a sharp core, $0.''6 < \mathrm{FWHM} < 1.''4$, as a "star." The number of "stars" found each night ranged from about 20,000 to about 100,000, depending on the exposure time and seeing.

The Suprime-Cam field is wide enough that even small uncorrected distortions near the edge of the field might move the apparent position of a star enough from one epoch to the next to hide real, but small, proper motions. In order to reduce any residual distortions, we broke the field into smaller units we will call "sectors." Each sector is a square 1000×1000 pixels, or 202×202 arcseconds, on a side. We allowed a small overlap of 10 arcseconds between adjacent sectors so that stars near the edges would not be missed.

We designated one epoch, 2007 February 15, as "fiducial," to serve as the basis of our matching procedure. For every other image, we used the *match* package (Droege et al. 2006)[3] to match the objects in each sector to objects in the corresponding sector of the fiducial image. In order to count as an initial match to the fiducial image, a star had to lie within $1.''0$ of the position of an object in the fiducial frame; we imposed this limit in order to avoid spurious matches between unrelated objects. Given the six-year span of our survey, this places an upper limit of about $0.''17$ per year on our proper motion candidates. We may increase this limit to look for fast-moving objects in the future. We will demonstrate later (see Figure 6) that this requirement does not have a strong effect on the results.

There were typically three hundred to eight hundred pairs of matching items found within each sector. We transformed the (pixel) coordinates of each star to the (pixel) coordinates of the fiducial image in the following iterative manner. First, we used all the matched pairs in the sector to find the coefficients of a linear transformation

$$x' = A + Bx + Cy \tag{1}$$

$$y' = D + Ex + Fy \tag{2}$$

2 http://spiff.rit.edu/tass/xvista

3 http://spiff.rit.edu/match

via a least-squares technique. Next, we computed the residuals between the positions of the members of each pair in the fiducial coordinate system. We discarded pairs with large residuals; specifically, any pair with a residual more than 10 times the 35th percentile. We then went back to compute new coefficients of the linear transformation with the surviving pairs. We repeated this procedure three times in each sector. Ignoring a few sectors with very few objects, the mean residual difference in position for surviving items matched to the fiducial frame was $0\overset{''}{.}071$. However, most of the objects contributing to this residual, like most of the objects in each image, are faint, and some of the matches are spurious. The uncertainties in the positions of bright objects are considerably smaller, as we will show below.

We performed trials using a cubic transformation between the two coordinate systems, but found that the residuals were not significantly smaller than those based on a linear transformation.

The final steps in our matching procedure were to discard duplicate entries for objects in the overlapping areas between sectors, and to discard any objects which appeared in fewer than five epochs. The result was a set of positions in the fiducial coordinate system for objects appearing in at least five epochs. In order to estimate the uncertainty in the calculated positions, we computed the mean position of each objects in each coordinate (row and col) and its standard deviation; we then discarded measurements more than two standard deviations from the mean and recalculated mean and standard deviation. As shown in the first two rows of Table 3, the typical clipped standard deviation rose from $0\overset{''}{.}007$ for bright, unsaturated objects to $0\overset{''}{.}047$ for faint objects.

In order to create a sample of objects for which proper motions could be measured accurately, we selected all objects which appeared in the fiducial image and at least four others. A total of 79605 objects satisfied this requirement. Faint objects were less likely to be selected, since they might not be detected on nights with poor seeing. In order to check the completeness of this sample as a function of magnitude, we inserted a set of 1000 artificial stars with magnitudes ranging from $21 < i' < 27$ into the images. We then re-analyzed the entire set of images as before. Figure 1 shows the fraction of artificial stars which were detected and placed into the sample for further study. Since the fraction falls to 50% at $i' \simeq 25.5$, we estimate that our search may be considered complete to that magnitude.

We subjected this sample to a round of tests. For each coordinate, row and column, we made a linear fit to position as a function of Julian Date. Our fitting routine, following Press et al. (1992), provides values for the the slope b of this line, the 95 percent confidence interval ci in the value of the slope, and the scatter s_x around the line. The scatter is another estimate of the one-dimensional uncertainty in the position of a single measurement; we show its values in the lower rows of Table 3.

In order to verify that our fitting method yields both the correct motion and an appropriate uncertainty, we ran a Monte Carlo simulation. For each integer magnitude between $21 < i' < 25$, and for each value of 1-D annual proper motion $\mu = 0\overset{''}{.}01, 0\overset{''}{.}02, \ldots, 0\overset{''}{.}20$, we created 100 artificial stars. For

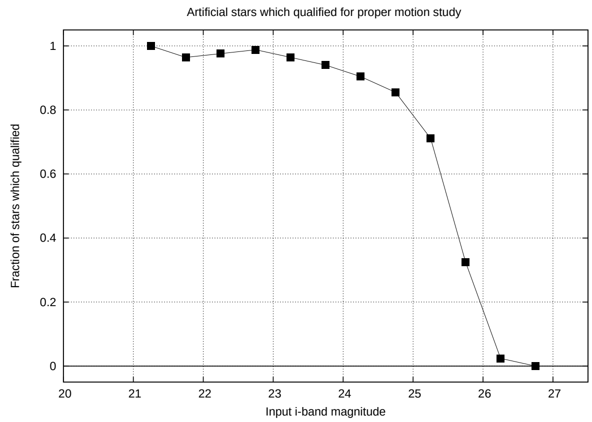

Fig. 1. Fraction of artificial stars added to the images which were detected and matched in at least 5 epochs.

each star, we drew 15 epochs randomly from our list of observations (see Table 2), and computed a set of positions, using the true proper motion plus some random error in each direction drawn from a gaussian distribution consistent with our measurements of s_x for the given magnitude. We then submitted this list of simulated positions to our fitting routines, and compared their results to the true proper motions. We found that over this entire range of magnitudes and motions, our estimates for the proper motion and its uncertainty were accurate.

Next, we computed a significance of the slope for each coordinate:

$$S_{row} \equiv \frac{b_{row}}{ci_{row}} \tag{3}$$

$$S_{col} \equiv \frac{b_{col}}{ci_{col}} \tag{4}$$

Choosing objects based on the significance of their motion in one direction alone would discriminate against objects moving diagonally across the CCD, which was aligned with the equatorial coordinate system. Therefore, we combined the significance values to create an unbiased measure of motion, $S_{tot} = \sqrt{S_{row}^2 + S_{col}^2}$.

We expect that real proper motions should show an asymmetry, due to the relative motions around the galactic center of the Sun and the stars in the SDF, while spurious motions due to random errors in position measurements should be the same in all directions. In the upper panel of Figure 2, we plot the observed motions of objects with motions of low significance; they are distributed around zero with circular symmetry. On the other hand, objects with highly significant motions (shown in the lower panel of Figure 2) are biased towards the south-east. The observed asymmetry matches that of the stars in a simulation made with the Besançon model (the motions of which we have scaled appropriately).

For the sample discussed below, we selected objects with $S_{tot} \geq 5.0$. Note that since our definition of S is based on a 95-percent confidence interval, corresponding to two standard deviations for a normal distribution, our criterion could be described as “motion at the 10-sigma level.” Selecting objects based on the S_{tot} statistic introduces a bias against objects with

Table 3. Estimates of uncertainty in position (arcsec) as function of i'-band mag

Sample, method	direction	$19-20$	$20-21$	$21-22$	$22-23$	$23-24$	$24-25$	$25-26$
All objects, clipped	row	0.010	0.006	0.006	0.007	0.012	0.028	0.047
stdev from mean pos	col	0.011	0.007	0.007	0.008	0.013	0.028	0.047
Moving candidates,	row	0.007	0.007	0.007	0.009	0.022	0.036	0.052
scatter from fit	col	0.008	0.008	0.009	0.011	0.023	0.036	0.052

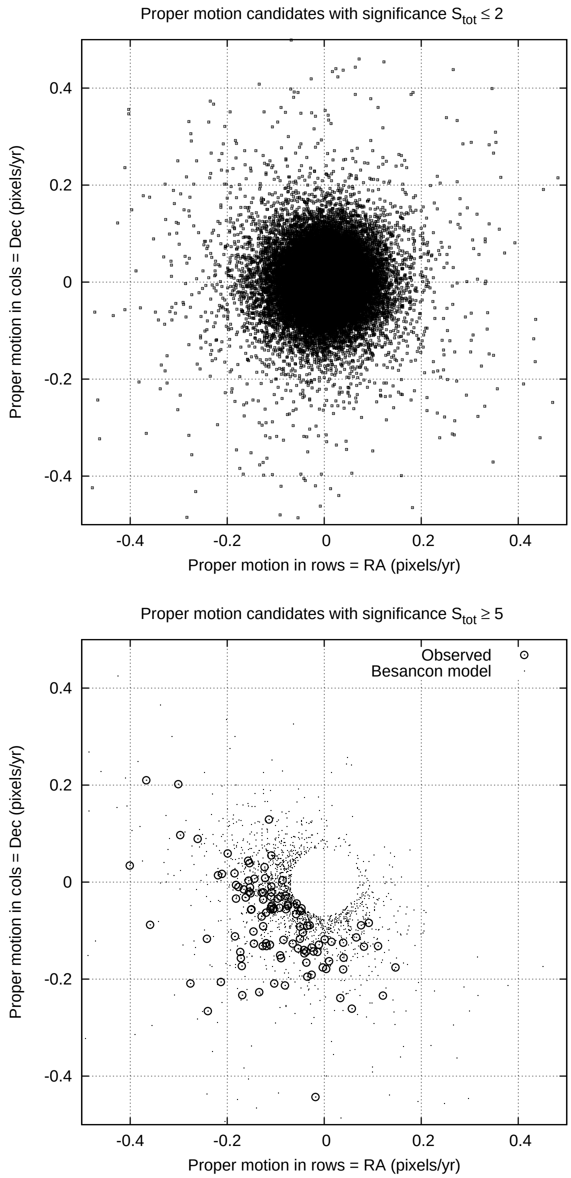

Fig. 2. Proper motions of objects with motions of small significance (top panel) and large significance (large circles in the bottom panel).

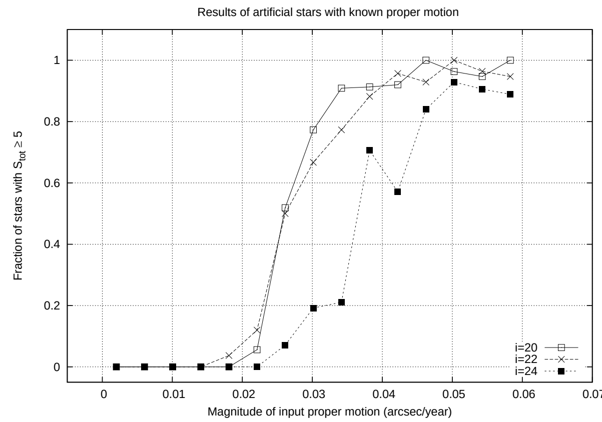

Fig. 3. Completeness test of the proper-motion sample using artificial stars.

small proper motions. We investigated the nature of this bias by adding artificial stars with a range of proper motions into our images, analyzing the images as before, and comparing the output properties of the artificial stars to their input values. In Figure 3, we show the fraction of artificial stars which had measured motions of high enough significance to be included in our proper motion sample. For bright stars, the fraction drops to 50% at a total proper motion of about $\mu = 0\farcs025$ per year.

We found that 110 objects passed this test. However, upon visually inspecting each candidate, we discovered that in five cases, the motions were due to a blend of two nearby stars, or a star mixed with the light of a background galaxy. That left a set of 105 candidates with real motions at a high significance. The median number of epochs of measurement for these objects was 19, and only 2 stars had fewer than 15 epochs. We show an example of the motions for one of these candidates in Figure 4.

How accurate are the derived motions? Using our set of artificial stars again, we computed a fractional error E based on the one-dimensional motion of stars in row and column directions separately.

$$E \equiv \frac{(\text{measured } \mu) - (\text{input } \mu)}{|\text{input } \mu| + Q} \tag{5}$$

We included a constant $Q = 0\farcs001$ per year to prevent division by zero. Figure 5 shows the median value of E as a function of input proper motion for stars of different magnitudes. The fractional error reaches 10% for proper motions of about $\mu = 0\farcs025$ per year.

Let us turn back to the real stars in the SDF. Figure 6 shows that the distribution of proper motions among stars in our sam-

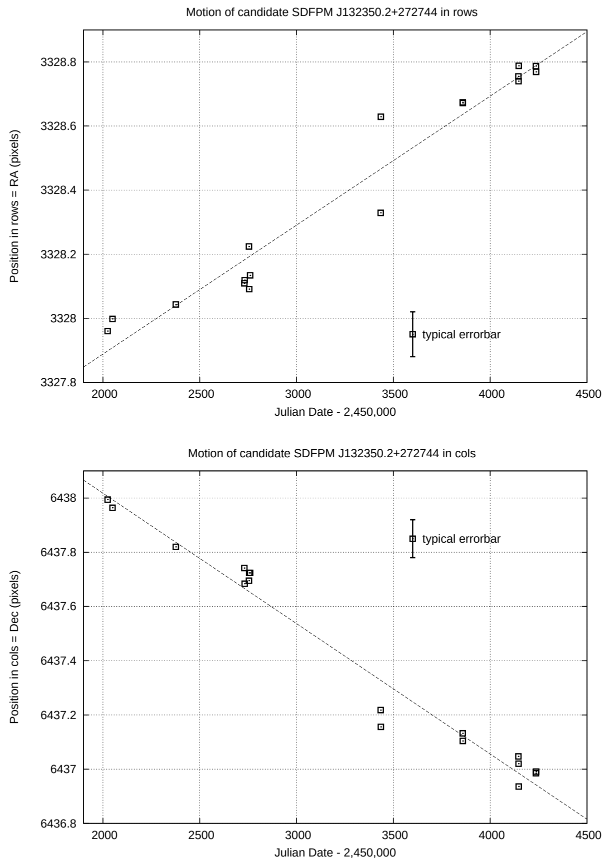

Fig. 4. An example of the motions for one of the candidates with high significance.

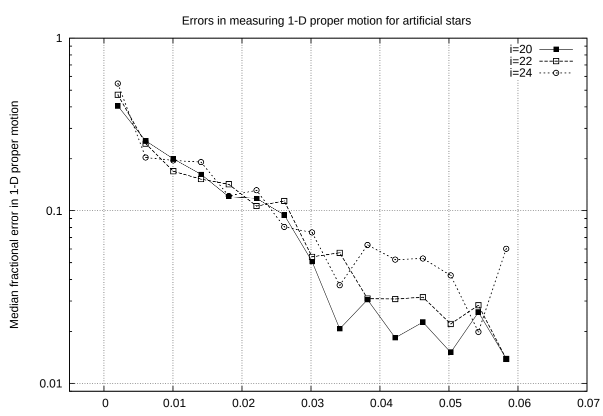

Fig. 5. Fractional errors in derived one-dimensional proper motions using artificial stars.

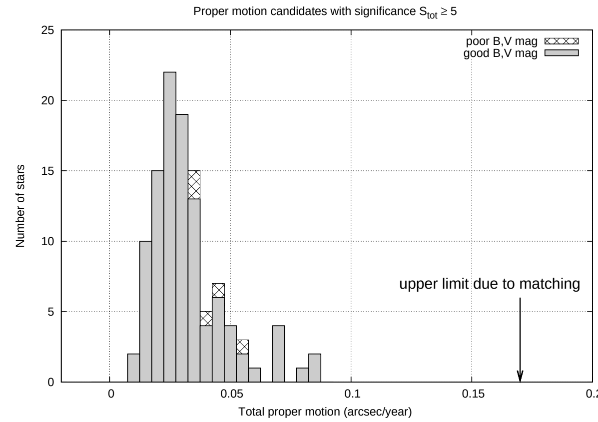

Fig. 6. Distribution of proper motions for candidates with high significance.

ple has a peak at $\mu = 0.^{\prime\prime}025$ per year, which is (not coincidentally) the point at which the efficiency of detecting motion falls to 50%. The largest motions we found are about $0.^{\prime\prime}09$ per year, which is far less than the limit of $0.^{\prime\prime}17$ per year set by our matching procedure. We conclude that our matching requirement – that each measurement lie within $1.^{\prime\prime}0$ of its match in the fiducial epoch – does not have a strong effect on the resulting proper motions.

Some of the analysis described below requires the color of an object, in order to distinguish different types of star. We chose the $(V - I)$ color for several reasons: it samples a wide range of wavelengths, avoids B-band measurements which are hard to make for cool stars, is often used in studies of galactic structure, and is commonly tabulated in models of stellar properties. Since we used i'-band images to search for motions, all the candidates had good i'-band magnitudes; we will convert them to the standard Cousins I system in the next paragraph. However, many of the candidates grow faint in images taken at shorter wavelengths. We inspected each candidate in deep SDF images (Kashikawa et al. 2004) taken in B, V and R_C passbands, and compared its appearance in those images to the B, V and R_C magnitudes listed for each object in the SDF catalogs. In six cases, the V-band measurement was clearly incorrect, sometimes due to confusion with a brighter object nearby; the number of improper magnitudes was much larger in B-band. Removing these six objects from our sample, we are left with a set of 99 stars which have well measured proper motions and good magnitudes in V, R_C, i' and z'. We call this our "first sample." We list these candidates in Table 4.

Before we can compare our measurements to models of galactic structure, we need to convert the Suprime-Cam i' magnitudes, which are calibrated on the AB system (Fukugita et al. 1996; Miyazaki et al. 2002; Kashikawa et al. 2004), to I magnitudes, which are on the standard Johnson-Cousins system. We used synthetic photometry to find the relationship between the Suprime-Cam $(V_s - i')$ and Johnson-Cousins $(V - I)$, taking bandpasses from Miyazaki et al. (2002) and Bessell (1990), respectively. We selected main sequence stars, O5V to M6V, from the library of Pickles (1998), stars ranging in metallicity $-2 \leq [\mathrm{Fe/H}] \leq 0$ from models of Lejeune et al.

(1997), and flux-calibrated spectra of white dwarfs observed by the SDSS (Adelman-McCarthy et al. 2008). We convolved each spectrum with the Suprime-Cam passbands and with the Johnson-Cousins passbands to compute synthetic magnitudes, and used the spectrum of Vega from Bohlin & Gilliland (2004) to set the zeropoints to the values given in Fukugita et al. (1996). We found that the following linear relationship fit the data well, yielding a scatter of less than 0.03 mag across the range of colors $-0.3 < (V-I) < 3.5$:

$$(V-I) = 0.391 + 1.1145(V_s - i') \qquad (6)$$

We use this equation to convert the observed colors for stars in the SDF to Johnson-Cousins $(V-I)$ when comparing our results to stellar models.

4. Simple analysis of the first sample

We begin with the Besançon model. We generated 10 simulated catalogs of objects in the area of the SDF, using the parameters found by Robin et al. (2003) and including stars down to an apparent magnitude of $V = 30$. We applied cuts to the synthetic catalogs to match the combined limits of the i'-band proper motion images and the SDF catalogs.

$$V \leq 26.0 \qquad (7)$$

$$I \leq 25.4 \qquad (8)$$

$$0\overset{''}{.}014 \leq \mu \leq 0\overset{''}{.}17 \qquad (9)$$

The result should be a set of stars similar to those in the actual SDF, though ten times more numerous. The large size of this synthetic sample will make it easier to delineate sparsely populated regions in the reduced proper motion diagram, to which we now turn.

Reduced proper motion was introduced by Luyten (1922) as a way to separate stars of different luminosities using only the observable apparent magnitude, m, and proper motion, μ, in units of arcseconds per year. We will base our reduced proper motion on V-band magnitudes, so that

$$H_V = m_V + 5\log(\mu) + 5 \qquad (10)$$

It is also possible to express this quantity in terms of a star's absolute magnitude, M, and tangential velocity, v_t, expressed in units of km/s,

$$H_V = M_V + 5\log(v_t) - 3.378 \qquad (11)$$

Using this version of the formula, we compute H_V for stars in the simulated catalogs produced from the Besançon model. Figure 7 shows the reduced proper motion as a function of $(V-I)$ color. We assigned objects in the simulation to three populations based on their metallicity and the component of their space velocity in the direction of galactic rotation, which we denote as vgr to avoid confusion with the passband V.

- if $vgr < -130$ km/s and $[Fe/H] < -1.20$, we assign the star to the **halo**
- if $vgr > -60$ km/s and $[Fe/H] > -0.50$, we assign the star to the **thin disk**
- otherwise, we assign the star to the **thick disk**

Stars from different populations appear in distinct regions in this diagram. We have drawn rough outlines by hand to aid the reader in recognizing the populations.

Note that there is a clear "red edge" in the distribution of WDs, at a color of $(V-I) \sim 1.4$. Theoretical models of cooling WDs (Richer et al. 2000; Chabrier et al. 2000) indicate that at an age of about 10 Gyr and a temperature of $T_{eff} \sim 5000$ K, an increase in opacity due to molecular hydrogen causes the $(V-I)$ color to shift back to the blue as the star continues to cool. WDs with atmospheres dominated by other elements, such as helium or carbon, would continue to grow redder as they cool. Objects near the bottom of the WD region are likely to be members of the halo.

In Figure 8, we present the reduced proper motions for the real stars in our first sample. We must switch to the first form of reduced proper motion, Equation 7, to compute H_V for the observed stars. To facilitate comparison with the Besançon model, we include the hand-drawn regions from Figure 7 as well as all objects from the simulated catalogs as tiny points. Note that the saturation of very bright stars $V \lesssim 20$ in the Subaru images, plus our limited ability to measure proper motions $\mu \lesssim 0\overset{''}{.}02$ per year, combine to eliminate any candidates with reduced proper motions $H \lesssim 16.5$. In the discussion which follows, please recall that the boundaries of the regions drawn in the diagram are only approximations intended to provide rough classifications; the number of items within each region could change by ten or twenty percent if one shifted the boundaries slightly.

Our 99 proper motion (PM) candidates divide into four groups: 9 fall inside the WD region, 43 inside the halo region, 23 in the disk region, and 24 lie in an area which had no stars in the Besançon model. Let us discuss the WD candidates first, and then consider the objects in the "empty" area.

The PM candidates falling into the WD region are concentrated near the red edge of the region, just as models of WD cooling predict. We take the combined results for ten simulated catalogs generated from the Besançon model, correct for completeness as a function of magnitude and proper motion, based on our tests with artificial stars (see Figure 3), and divide by 10 to find predictions of 2.2 WDs in the halo, 5.9 in the thick disk and 0.7 in the thin disk, for a total of 8.8 WDs satisfying our selection criteria in the SDF. Our sample yields 9 candidates in this region, consistent with the model. Note that several candidates lie just outside the WD region; we must make additional measurements of these objects before we can make any confident claim about the exact number of WDs. Which of our candidates are most likely to be members of the halo? As a young WD cools, it slides diagonally down and to the right on this diagram, parallel to the lower envelope of the simulation's objects. Due to their high velocities, halo WDs should lie near the bottom of the distribution. There are several candidates at some distance below the main locus of simulation objects; we believe the two at $H_V = 23.0$ and $H_V = 24.2$ are the most likely of our candidates to be halo dwars.

Roughly one-quarter of our PM candidates lie in an "empty" region between the simulation's WD and halo stars. Since we drew the boundaries by hand, they may certainly be shifted by small amounts; that would cause a number of the anamolous

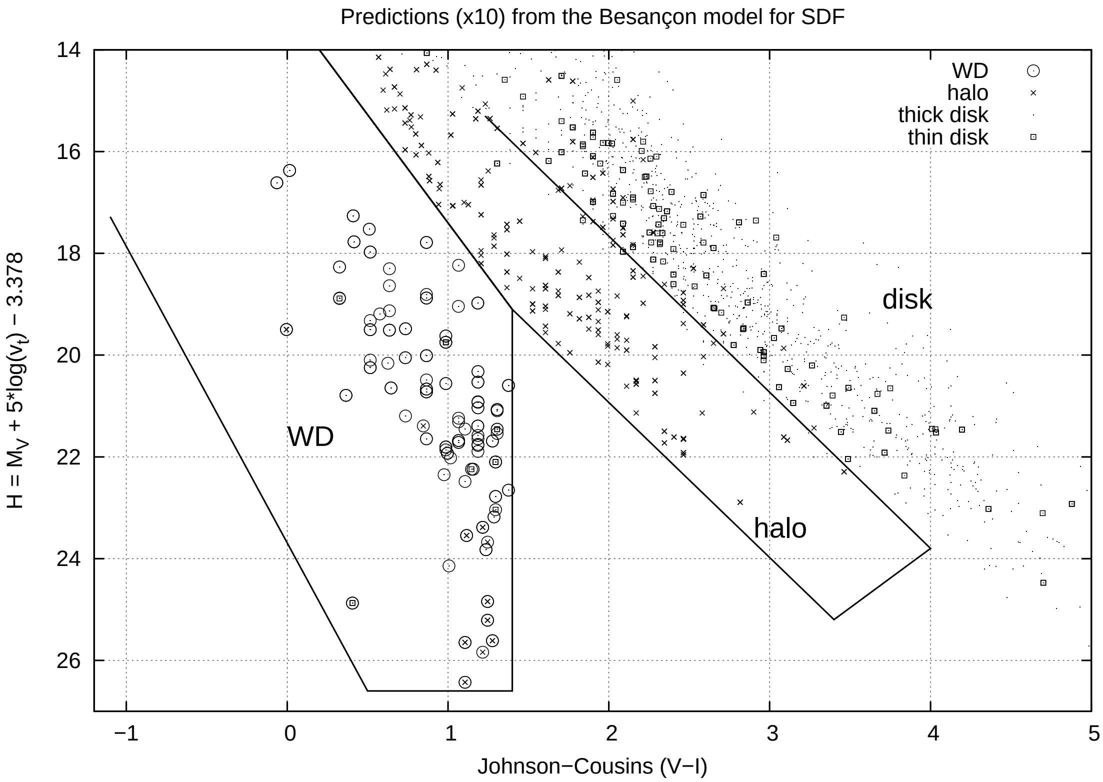

Fig. 7. Reduced proper motion diagram for objects in simulated catalogs created with the Besançon model

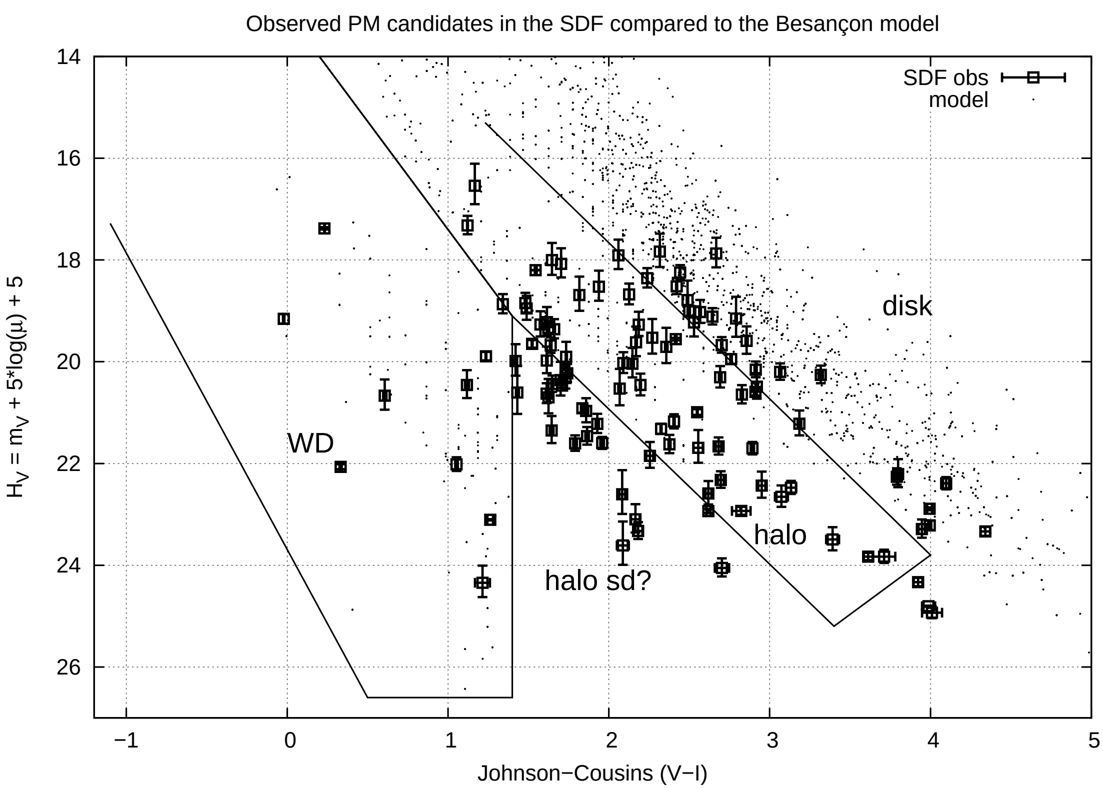

Fig. 8. Reduced proper motion diagram for real objects observed in the SDF. The regions are identical to those in Figure 7. Each measurement has errorbars in both directions, though some are too small to see.

objects to fall within the halo or WD regions. However, some of our candidates are more than one magnitude away from any population in the simulations. Is it possible that they may be ordinary stars reddened by dust? According to Schlegel et al. (1998), dust along the line of sight through the SDF should produce $E(B-V)=0.015$ mag; the corresponding extinction, $A_V = 0.051$ and $A_I = 0.030$, is too small to shift candidates a significant distance in the reduced PM diagram. We suggest that these objects may be metal-poor subdwarfs in the halo, a class of star which is not included in the Besançon model. If we make an HR diagram using M_V and $(V-I)$, we find that the halo stars in the Besançon model cross the disk main sequence in the range $1.5 < (V-I) < 3.0$, and are slightly more luminous in the redder portion of this range. However, as Reid & Gizis (1998) show, extremely metal-poor subdwarfs are much fainter than disk stars in this color range, by up to 4 magnitudes. Stars with these photometric properties and halo kinematics would lie several magnitudes below the halo region drawn in our diagrams. We therefore tentatively identify as extremely metal-poor halo stars the PM candidates which fall far from the WD and halo regions.

5. Future work

Our first step will be to acquire spectra of some of our PM candidates to verify their identity as WDs and metal-poor subdwarfs. After we have spectra for a good fraction of our candidates, we can assign types to the candidates with more confidence. At that point, we will make a more detailed and quantitative comparison of the WDs in our sample with those expected from models of the Milky Way.

We can also look at candidates with motions of somewhat lower significance. In this paper, we examined the 110 stars which had $S_{tot} > 5.0$. There were 72 stars with $4.0 \le S_{tot} < 5.0$, and they show nearly the same degree of asymmetry in their motions as our first sample. It is likely that a significant number of these stars have real proper motions. However, it will take extra effort to distinguish them from the growing number of false detections, and to check their photometry (many of them are fainter than the stars in our sample). As we sift through this set of stars with less significant motions, we can also try to improve the B and V measurements of our stars, so that we will not discard so many candidates due to their uncertain colors.

Finally, we can apply the same techniques to find stars with large proper motions in other deep fields with multiple visits by Subaru. Our next target will be the area of the Subaru/XMM-Newton Deep Survey (Sekiguchi et al. 2004, Furusawa et al. 2008), which is roughly in the opposite direction from the SDF. We can use it to check our results in the SDF, but also to look for differences predicted by models of galactic populations.

We thank the staff at the Subaru Telescope for their assistance with the observations used in this project. MWR gratefully acknowledges grant S-03031 from the JSPS Invitation Fellowship for Research in Japan. This work is supported in part by a JSPS core-to-core program "International Research Network for Dark Energy" and by a JSPS research grant (17104002). Long ago, Charles Alcock suggested that we use Suprime-Cam to search for white dwarfs; we are glad to be putting his idea into practice at last. A.G. acknowledges support by the Benoziyo Center for Astrophysics and the William Z. and Eda Bess Novick New Scientists Fund at the Weizmann Institute.

Funding for the Sloan Digital Sky Survey (SDSS) and SDSS-II has been provided by the Alfred P. Sloan Foundation, the Participating Institutions, the National Science Foundation, the U.S. Department of Energy, the National Aeronautics and Space Administration, the Japanese Monbukagakusho, and the Max Planck Society, and the Higher Education Funding Council for England. The SDSS Web site is http://www.sdss.org/.

The SDSS is managed by the Astrophysical Research Consortium (ARC) for the Participating Institutions. The Participating Institutions are the American Museum of Natural History, Astrophysical Institute Potsdam, University of Basel, University of Cambridge, Case Western Reserve University, The University of Chicago, Drexel University, Fermilab, the Institute for Advanced Study, the Japan Participation Group, The Johns Hopkins University, the Joint Institute for Nuclear Astrophysics, the Kavli Institute for Particle Astrophysics and Cosmology, the Korean Scientist Group, the Chinese Academy of Sciences (LAMOST), Los Alamos National Laboratory, the Max-Planck-Institute for Astronomy (MPIA), the Max-Planck-Institute for Astrophysics (MPA), New Mexico State University, Ohio State University, University of Pittsburgh, University of Portsmouth, Princeton University, the United States Naval Observatory, and the University of Washington.

References

Adelman-McCarthy, J. et al. 2008, ApJS, 175, 297
Bessell, M. S. 1990, PASP, 102, 1181
Bohlin, R. C. & Gilliland, R. L. 2004, AJ, 127, 3508
Carollo, D. et al. 2006, A&A, 448, 579
Chabrier, G. et al. 2000, ApJ, 543, 216
Droege, T. F. et al. 2006, PASP, 118, 1666
Fukugita, M. et al. 1996, AJ, 111, 1748
Furusawa, H. et al. 2008, ApJS, 176, 1
Ibata, R. et al. 2007, ApJ, 671, 1591
Juric, M. et al. 2008, ApJ, 673, 864
Liebert, J. et al. 1988, ApJ, 332, 891
Kashikawa, N. et al. 2004, PASJ, 56, 1011
Kalirai, J. S. et al. 2004, ApJ, 601, 277
Lejeune, T., Cuisinier, F., & Buser, R. 1997, A&AS, 125, 229
Luyten, W. J. 1922, PASP, 34, 54
Mendez, R. A. 2002, A&A, 395, 779
Miyazaki, S. et al. 2002, PASJ, 54, 833
Nagao, T. et al. 2004, ApJ, 613, 9
Nelson, C. A. et al. 2002, ApJ, 573, 644
Oppenheimer, B. R. et al. 2001, Science, 292, 698
Ouchi, M. et al. 2004, ApJ, 611, 660
Patel, K. C. & Spath, S. R. 2004, SPIE, 5487, 112
Pickles, A. J. 1998, PASP, 110, 863
Poznanski, D. et al. 2007, MNRAS, 382, 1169
Press, W. H., Flannery, B. P. & Teukolsky, S. A. 1986, "Numerical Recipes in C: The Art of Scientific Computing," (Cambridge: Cambridge University Press)
Reid, I. N. 2005, ARA&A, 43, 247
Reid, I. N. & Gizis, J. E. 1998, AJ, 116, 2929
Richer, H. B. 2000, ApJ, 529, 318

Robin, A. C., Reylé, C., Derrière, S., & Picaud, S. 2003, A&A, 409, 523
Richmond, M. W. 2005, PASJ, 57, 969
Schlegel, D. J., Finkbeiner, D. P., & Davis, M. 1998, ApJ, 500, 525
Sekiguchi, K. et al. 2004, BAAS, 205, 8105
Shimasaku, K. et al. 2006, PASJ, 58, 313
Skrutskie, M. F. et al. 2006, AJ, 131, 1163
Stone, R. C. 1989, AJ, 97, 1227
Treffers, R. R. & Richmond, M. W. 1989, PASP, 101, 725
Yanny, B. et al. 2000, ApJ, 540, 825
Yagi, M. et al. 2002, AJ, 123, 66

Table 4. First sample of proper motion candidates in the SDF

ID	RA*	Dec*	V^{**}	$R_c{}^{**}$	i'^{**}	z'^{**}	RA PM†	Dec PM†
SDFPM J132339.4+271916	200.91424	27.32130	21.784	21.025	20.164	19.607	-0.049 ± 0.004	-0.024 ± 0.004
SDFPM J132343.5+272230	200.93138	27.37519	20.889	20.198	19.501	18.853	-0.034 ± 0.004	-0.003 ± 0.006
SDFPM J132343.6+272753	200.93170	27.46494	22.821	21.995	20.868	20.265	-0.017 ± 0.002	0.001 ± 0.004
SDFPM J132346.9+274556	200.94582	27.76573	21.810	20.993	20.003	19.425	-0.073 ± 0.004	-0.018 ± 0.004
SDFPM J132347.5+271829	200.94827	27.30829	21.711	21.005	20.505	20.139	-0.037 ± 0.004	-0.023 ± 0.004
SDFPM J132348.0+273232	200.95033	27.54234	24.208	23.350	22.209	21.615	-0.053 ± 0.002	0.018 ± 0.002
SDFPM J132348.0+273702	200.95029	27.61729	23.585	22.739	21.520	20.867	-0.022 ± 0.002	-0.002 ± 0.002
SDFPM J132350.2+272744	200.95944	27.46232	19.051	19.110	19.193	19.141	0.030 ± 0.004	-0.036 ± 0.004
SDFPM J132351.0+273453	200.96275	27.58148	21.617	20.713	19.596	18.739	0.017 ± 0.002	-0.027 ± 0.004
SDFPM J132353.1+272759	200.97157	27.46647	23.648	22.870	22.073	21.626	-0.006 ± 0.002	-0.018 ± 0.002
SDFPM J132353.4+272207	200.97253	27.36882	20.417	19.870	19.564	19.130	-0.034 ± 0.004	-0.035 ± 0.002
SDFPM J132354.0+272806	200.97518	27.46843	24.444	23.488	21.818	20.910	-0.012 ± 0.000	-0.009 ± 0.002
SDFPM J132354.3+273016	200.97647	27.50454	23.857	23.334	22.733	22.322	-0.032 ± 0.004	0.001 ± 0.004
SDFPM J132354.5+273356	200.97722	27.56561	22.793	22.390	22.199	22.029	-0.056 ± 0.004	-0.042 ± 0.002
SDFPM J132356.7+274445	200.98637	27.74593	22.248	21.560	21.150	20.835	-0.024 ± 0.004	-0.025 ± 0.002
SDFPM J132357.5+271458	200.98977	27.24948	23.025	22.144	20.812	20.046	-0.019 ± 0.002	-0.007 ± 0.002
SDFPM J132400.0+273750	201.00007	27.63083	21.997	21.169	20.115	19.443	-0.009 ± 0.000	-0.021 ± 0.004
SDFPM J132401.1+273613	201.00494	27.60384	23.932	23.034	21.688	20.989	-0.036 ± 0.002	-0.002 ± 0.002
SDFPM J132402.5+272639	201.01074	27.44421	25.483	24.796	23.022	22.008	0.003 ± 0.002	-0.025 ± 0.002
SDFPM J132403.6+271314	201.01540	27.22081	24.830	24.027	23.312	22.843	-0.024 ± 0.004	-0.027 ± 0.006
SDFPM J132403.6+273833	201.01540	27.64265	22.152	21.247	19.998	19.174	-0.022 ± 0.004	-0.011 ± 0.002
SDFPM J132404.5+272557	201.01911	27.43275	24.593	23.464	21.534	20.563	-0.033 ± 0.004	-0.006 ± 0.002
SDFPM J132404.5+273829	201.01897	27.64141	23.774	23.016	22.452	22.084	-0.023 ± 0.002	-0.026 ± 0.002
SDFPM J132407.4+272751	201.03110	27.46440	23.326	22.556	22.030	21.693	-0.032 ± 0.002	0.009 ± 0.002
SDFPM J132407.4+272924	201.03107	27.49026	20.825	20.089	19.268	18.488	0.008 ± 0.002	-0.036 ± 0.004
SDFPM J132407.8+273621	201.03275	27.60605	20.992	20.211	19.334	18.498	-0.011 ± 0.002	-0.028 ± 0.002
SDFPM J132408.0+274455	201.03344	27.74886	23.205	23.035	23.011	22.952	-0.031 ± 0.004	-0.005 ± 0.002
SDFPM J132409.7+273406	201.04050	27.56846	22.629	21.914	21.501	21.195	-0.018 ± 0.002	-0.032 ± 0.002
SDFPM J132411.1+271310	201.04634	27.21970	21.478	20.735	19.868	19.261	0.001 ± 0.002	-0.036 ± 0.004
SDFPM J132412.6+272220	201.05261	27.37244	21.385	20.713	20.279	19.940	-0.005 ± 0.002	-0.039 ± 0.002
SDFPM J132413.0+272651	201.05433	27.44771	21.211	20.568	20.195	19.890	0.007 ± 0.002	-0.048 ± 0.002
SDFPM J132413.2+273139	201.05511	27.52759	24.476	23.966	23.694	23.519	0.024 ± 0.004	-0.047 ± 0.002
SDFPM J132413.5+271547	201.05657	27.26317	23.270	22.586	22.068	21.668	-0.010 ± 0.002	-0.024 ± 0.002
SDFPM J132415.4+271328	201.06428	27.22462	23.341	22.562	21.837	21.368	-0.024 ± 0.004	-0.013 ± 0.002
SDFPM J132415.9+271624	201.06654	27.27336	21.285	21.492	21.654	21.798	-0.037 ± 0.002	0.004 ± 0.004
SDFPM J132418.0+271902	201.07534	27.31740	20.754	20.099	19.576	19.011	-0.029 ± 0.004	0.001 ± 0.004
SDFPM J132419.4+273411	201.08115	27.56974	23.404	22.691	22.296	21.994	-0.013 ± 0.002	-0.026 ± 0.004
SDFPM J132423.6+274031	201.09851	27.67550	24.878	24.092	22.810	22.094	-0.008 ± 0.002	-0.030 ± 0.002
SDFPM J132423.7+274425	201.09904	27.74048	24.684	23.560	21.358	20.143	-0.023 ± 0.002	0.026 ± 0.004
SDFPM J132425.8+272415	201.10777	27.40424	22.134	21.348	20.242	19.579	0.015 ± 0.004	-0.018 ± 0.002
SDFPM J132427.4+271919	201.11456	27.32220	21.667	20.920	19.939	19.277	-0.016 ± 0.002	-0.006 ± 0.002
SDFPM J132427.5+274302	201.11464	27.71747	21.899	21.050	19.979	19.326	-0.004 ± 0.000	-0.029 ± 0.004
SDFPM J132429.2+273817	201.12177	27.63832	22.417	21.510	20.291	19.581	-0.031 ± 0.002	0.008 ± 0.002
SDFPM J132429.7+273932	201.12378	27.65908	23.801	23.352	23.149	22.980	-0.019 ± 0.002	-0.011 ± 0.002
SDFPM J132429.8+274304	201.12447	27.71788	24.576	23.709	22.521	21.894	-0.002 ± 0.002	-0.026 ± 0.002
SDFPM J132430.6+272406	201.12789	27.40185	25.066	24.034	22.769	22.151	-0.026 ± 0.002	-0.014 ± 0.004
SDFPM J132430.9+273624	201.12897	27.60693	23.844	23.145	22.437	22.015	-0.001 ± 0.002	-0.036 ± 0.002
SDFPM J132431.3+271528	201.13047	27.25786	23.296	22.392	21.111	20.377	-0.008 ± 0.002	-0.028 ± 0.002
SDFPM J132431.9+272236	201.13305	27.37668	20.942	20.325	19.957	19.596	-0.007 ± 0.002	-0.039 ± 0.004
SDFPM J132432.0+273510	201.13343	27.58623	26.614	25.586	23.635	22.704	-0.005 ± 0.002	-0.027 ± 0.002
SDFPM J132432.9+274301	201.13713	27.71701	21.809	21.082	20.626	20.313	0.012 ± 0.004	-0.053 ± 0.002
SDFPM J132434.5+271432	201.14385	27.24230	21.333	20.533	19.396	18.506	-0.074 ± 0.006	0.042 ± 0.006
SDFPM J132435.0+271638	201.14597	27.27749	24.078	23.314	22.761	22.360	-0.022 ± 0.002	-0.010 ± 0.002
SDFPM J132436.5+272345	201.15221	27.39585	25.624	24.331	22.079	20.895	0.022 ± 0.004	-0.027 ± 0.002
SDFPM J132438.0+273622	201.15867	27.60634	20.594	20.088	19.836	19.525	-0.048 ± 0.002	-0.054 ± 0.002

Table 4. (Continued.)

SDFPM J132438.4+273433	201.16001	27.57608	25.234	24.507	23.642	23.123	-0.037 ± 0.004	-0.007 ± 0.006
SDFPM J132438.8+272847	201.16168	27.47980	21.242	20.387	19.401	18.580	0.019 ± 0.004	-0.017 ± 0.002
SDFPM J132439.0+272413	201.16284	27.40377	21.748	20.978	20.063	19.473	-0.029 ± 0.004	-0.021 ± 0.004
SDFPM J132439.2+273949	201.16367	27.66381	25.890	25.991	23.708	22.493	-0.025 ± 0.002	0.006 ± 0.002
SDFPM J132440.4+272911	201.16870	27.48653	20.569	20.101	19.872	19.567	-0.010 ± 0.002	-0.012 ± 0.002
SDFPM J132440.6+272548	201.16954	27.43018	25.902	25.050	23.210	22.293	0.002 ± 0.002	-0.033 ± 0.004
SDFPM J132440.7+271501	201.16992	27.25041	20.436	20.017	19.781	19.510	0.000 ± 0.002	-0.024 ± 0.002
SDFPM J132444.4+273945	201.18514	27.66254	23.530	22.957	22.607	22.279	-0.016 ± 0.002	-0.011 ± 0.002
SDFPM J132444.9+272709	201.18741	27.45264	22.431	21.622	20.613	20.051	0.013 ± 0.004	-0.023 ± 0.002
SDFPM J132446.0+272605	201.19208	27.43499	22.250	21.553	21.112	20.813	-0.026 ± 0.002	-0.004 ± 0.002
SDFPM J132446.8+274114	201.19519	27.68733	24.778	23.590	21.544	20.448	-0.040 ± 0.002	0.012 ± 0.004
SDFPM J132447.0+272814	201.19610	27.47077	23.045	22.143	20.783	20.064	0.008 ± 0.000	-0.025 ± 0.002
SDFPM J132447.8+272157	201.19930	27.36586	23.236	22.290	20.836	19.993	-0.025 ± 0.002	0.002 ± 0.002
SDFPM J132448.1+272803	201.20046	27.46761	21.790	21.173	20.812	20.554	-0.025 ± 0.002	-0.004 ± 0.002
SDFPM J132448.6+272747	201.20255	27.46314	25.725	24.967	23.319	22.436	-0.022 ± 0.002	-0.010 ± 0.002
SDFPM J132448.8+273205	201.20361	27.53479	21.771	20.993	20.036	19.427	-0.081 ± 0.004	0.007 ± 0.002
SDFPM J132449.7+274510	201.20714	27.75295	25.447	24.324	22.278	21.207	-0.043 ± 0.002	-0.042 ± 0.002
SDFPM J132451.7+273110	201.21556	27.51972	25.980	25.510	25.241	24.948	-0.021 ± 0.008	-0.042 ± 0.004
SDFPM J132452.1+271813	201.21743	27.30386	24.103	23.165	21.596	20.792	-0.025 ± 0.002	-0.007 ± 0.004
SDFPM J132453.1+271821	201.22154	27.30592	22.338	21.642	21.242	20.944	-0.035 ± 0.002	-0.029 ± 0.004
SDFPM J132454.0+274226	201.22508	27.70739	23.462	22.682	21.698	21.148	-0.012 ± 0.002	-0.013 ± 0.002
SDFPM J132455.3+272957	201.23056	27.49939	25.095	24.307	23.423	22.968	-0.022 ± 0.002	-0.004 ± 0.004
SDFPM J132456.0+274126	201.23345	27.69078	25.805	24.801	22.578	21.065	-0.060 ± 0.002	0.020 ± 0.002
SDFPM J132456.1+272807	201.23412	27.46872	22.942	22.059	20.673	19.936	-0.030 ± 0.004	-0.011 ± 0.000
SDFPM J132458.1+272326	201.24241	27.39072	23.633	22.700	21.372	20.676	-0.022 ± 0.002	0.011 ± 0.002
SDFPM J132459.8+271251	201.24932	27.21436	23.548	22.849	22.374	21.961	-0.022 ± 0.002	-0.006 ± 0.006
SDFPM J132500.3+272357	201.25147	27.39927	22.401	21.675	21.122	20.775	-0.015 ± 0.002	-0.010 ± 0.002
SDFPM J132503.8+273938	201.26620	27.66072	21.497	20.741	19.999	19.479	-0.018 ± 0.002	-0.006 ± 0.002
SDFPM J132504.6+273028	201.26917	27.50779	21.614	20.808	19.792	19.074	-0.021 ± 0.002	-0.011 ± 0.000
SDFPM J132505.4+273731	201.27253	27.62530	22.684	21.943	21.160	20.728	-0.017 ± 0.002	-0.024 ± 0.002
SDFPM J132505.3+271440	201.27212	27.24446	22.854	22.143	21.642	21.233	-0.007 ± 0.002	-0.029 ± 0.002
SDFPM J132505.5+273401	201.27318	27.56696	22.398	21.772	21.336	21.058	-0.021 ± 0.002	-0.011 ± 0.002
SDFPM J132506.1+273816	201.27567	27.63800	21.999	21.309	20.880	20.594	-0.007 ± 0.002	-0.034 ± 0.002
SDFPM J132508.4+273553	201.28501	27.59830	20.672	20.018	19.546	19.011	-0.003 ± 0.002	-0.029 ± 0.004
SDFPM J132512.6+271620	201.30271	27.27244	22.398	21.731	21.362	21.034	-0.009 ± 0.000	-0.011 ± 0.000
SDFPM J132512.9+274045	201.30410	27.67940	25.443	24.610	23.500	22.863	-0.015 ± 0.002	-0.009 ± 0.002
SDFPM J132514.3+272421	201.30981	27.40588	21.422	20.499	19.379	18.486	-0.007 ± 0.002	-0.018 ± 0.002
SDFPM J132514.7+272642	201.31146	27.44522	23.121	22.559	22.187	21.881	-0.025 ± 0.004	-0.018 ± 0.006
SDFPM J132514.7+271707	201.31146	27.28543	22.993	22.180	21.211	20.640	-0.027 ± 0.002	-0.046 ± 0.004
SDFPM J132515.3+274212	201.31400	27.70335	22.304	22.297	22.357	22.406	-0.004 ± 0.004	-0.089 ± 0.002
SDFPM J132515.7+272708	201.31560	27.45226	24.696	23.629	21.645	20.570	-0.031 ± 0.002	-0.012 ± 0.002
SDFPM J132516.9+274518	201.32065	27.75507	23.660	22.886	22.281	21.891	0.008 ± 0.004	-0.032 ± 0.004
SDFPM J132521.1+271927	201.33814	27.32435	25.853	25.090	24.331	23.887	-0.018 ± 0.004	-0.031 ± 0.006
SDFPM J132525.4+273755	201.35591	27.63220	22.179	21.330	20.105	19.355	-0.031 ± 0.002	-0.004 ± 0.002
SDFPM J132527.7+274407	201.36559	27.73528	25.738	24.934	23.663	22.972	-0.016 ± 0.002	-0.043 ± 0.004
SDFPM J132527.7+272350	201.36576	27.39737	22.596	21.898	21.498	21.218	-0.010 ± 0.002	-0.019 ± 0.002
SDFPM J132528.3+274355	201.36796	27.73214	25.676	24.699	22.785	21.825	-0.043 ± 0.002	0.003 ± 0.002
SDFPM J132528.3+272012	201.36811	27.33679	22.163	21.424	20.568	20.040	-0.031 ± 0.004	-0.002 ± 0.002
SDFPM J132533.6+274708	201.39036	27.78563	23.894	22.665	20.660	19.533	-0.061 ± 0.008	0.041 ± 0.006
SDFPM J132533.9+272808	201.39152	27.46905	23.653	22.925	22.398	22.030	-0.029 ± 0.002	-0.026 ± 0.002

* Equinox J2000, epoch 2007.13.

** Corrected isophotal magnitudes from catalogs of Kashikawa et al. (2004).

† Proper motions in arcseconds per year.